

Boosting charge separation on epitaxial In_2O_3 octahedron-nanowire crystal facet-based homojunctions for robust photoelectrochemical water splitting

Ming Meng^{a,*}, Liwei Wang^a, Chunyang Li^a, Kun Xu^a, Yuanyuan Chen^a, Jitao Li^a, Zhixing Gan^b, Honglei Yuan^a, Lizhe Liu^{c,*}, Jun Li^{d,*}

^a School of Physics and Telecommunication Engineering, Zhoukou Normal University, Zhoukou 466001, PR China

^b Center for Future Optoelectronic Functional Materials, School of Computer and Electronic Information/School of Artificial Intelligence, Nanjing Normal University, Nanjing 210023, PR China

^c Department of Physics, Nanjing University, Nanjing 210093, PR China

^d Henan Institute of Advanced Technology, Zhengzhou University, Zhengzhou 450052, PR China



ARTICLE INFO

Keywords:

Homojunction
Crystal facet effect
Epitaxial growth
 In_2O_3 nanostructures
Photoelectrochemical water splitting

ABSTRACT

Hindering the recombination of photogenerated charges in photoelectrodes is extremely essential yet hugely challenging. Herein, the In_2O_3 homojunctions comprising of square nanowires exclusively enclosed by {001} facets and octahedrons fully surrounded by {111} facets are exemplified to illustrate a new strategy of crystal facet-induced charges separation. Kelvin probe force microscopy, spatially resolved surface photovoltage, photo-depositions and theoretical calculations corroborate that the oriented built-in electric field from {111} to {001} facets caused by work function difference of two facets render the photogenerated electrons and holes to accumulate on surface of octahedrons and nanowires, respectively, achieving the effective charges separation with long spatial distance. Benefiting from this advantage, the In_2O_3 crystal facet-based homojunctions exhibit dramatically higher photoelectrochemical water splitting activity compared with standalone nanowires, octahedrons and truncated octahedrons. The new strategy of boosting the charges separation can be extended to other applications such as photodetectors, solar cells and photocatalysis.

1. Introduction

Photoelectrochemical (PEC) water splitting has been deemed as an economical and sustainable strategy for directly converting and storing inexhaustible solar energy into energy-rich hydrogen fuel [1–9]. The efficiency of PEC water splitting of the semiconductor-based photo-electrode is largely dictated by its capability of hindering the surface and bulk recombination of photogenerated charges (photogenerated electrons and holes) [10–17]. Hence, tremendous efforts have been devoted toward promoting the photogenerated charges separation in semiconductor-based photoelectrodes [12–21]. Recent researchers have demonstrated that anisotropic facet electronic structures can create the build-in electrical field between the co-exposed crystal facets of single polyhedral micro/nanoparticles, which would drive the photogenerated electrons and holes to different crystal facets, respectively [22–27]. Moreover, some specific crystal facets not only offer highly active catalytic sites, but also generate the lower barrier at the semiconductor/electrolyte interface, significantly accelerating the surface

water splitting reactions [17,28,29]. All these attractive features furnish the opportunity to design the new excellent photoelectrodes, and thus the delicate maneuver of the crystal facets is meaningful and vital.

However, the existing investigations have mainly concentrated on the single polyhedral micro/nanoparticles, including TiO_2 [30,31], WO_3 [32,33], BiVO_4 [12–14], Fe_2O_3 [34,35], In_2O_3 [36–38], SrTiO_3 [39,40], where the charge separations occur only at the edge between the co-exposed facets [12,14,30–40]. As such, part of the photogenerated charges still encounter the unfavorable bulk and surface recombination due to the short spatial distance [17,41,42]. Accordingly, constructing the innovative crystal facet-based homojunctions via the two different crystal facets of two mutually independent micro/nanostructures has potential to circumvent the above undesired situation of the single polyhedral particles. Such structures render photogenerated electrons and holes to accumulate on the surface of the distinct micro-/nanostructures, respectively. In this case, photogenerated charges separation have a long spatial distance, which could effectively hinder their bulk and surface recombination. Nevertheless, the application of the

* Corresponding authors.

E-mail addresses: mengmingfly@163.com (M. Meng), lzliu@nju.edu.cn (L. Liu), junli2019@zzu.edu.cn (J. Li).

innovative crystal facet-based homojunctions as a photoanode for PEC water splitting has not been reported so far. The key obstacle lies in the experimental fabrication of such charming structures, since integrating the two distinct micro/nanostructures at one single structure involves two different growth behaviors/mechanisms and may necessitate different growth conditions [43]. This also implies the charges separation mechanism in the PEC water splitting reactions remains unclear for the innovative crystal facet-based homojunctions. Therefore, conquering the above problem paves a new avenue to promote the photogenerated charges separation, which can be extended to other applications such as photodetectors, solar cells and photocatalysis.

Herein, we present an innovative design and fabrication of the In_2O_3 homojunctions consisting of square nanowires exclusively enclosed by $\{001\}$ facets and octahedrons fully surrounded by $\{111\}$ facets. Cubic In_2O_3 was selected as the model catalyst on account of its proper band-edge position and superior PEC stability [36–38]. More importantly, its high symmetry confers it with diverse morphologies, which is an ideal platform material for constructing the innovative crystal facet-based homojunctions. The growth mechanism of the In_2O_3 crystal-facet-based homojunctions was systematically explored and its in-depth understanding was obtained. Additionally, Kelvin probe force microscopy (KPFM), spatially resolved surface photovoltage (SRSPV), photo-depositions and theoretical calculations corroborated that the oriented built-in electric field from $\{111\}$ to $\{001\}$ facet caused by work function difference of two facets allow photogenerated electrons and holes to accumulate on surface of octahedrons and nanowires, respectively, achieving the effective charges separation with long spatial distance. In addition, the well-matched lattice fringes between the In_2O_3 epitaxial octahedron and nanowire serve as the convenient and fast channel for the charge transfer between two sections of homojunction, further accelerating the charges separation. Benefiting from these advantages, the innovative In_2O_3 crystal facet-based homojunctions grown at optimal condition delivered a photocurrent density of 1.42 mA/cm^2 at 0.22 V vs. Ag/AgCl , nearly 7.1 and 28.4 times those of standalone nanowires and octahedrons, respectively. This value is also higher than that of the In_2O_3 truncated octahedrons (0.4 mA/cm^2), namely traditional crystal facet-based homojunctions.

2. Experimental section

2.1. Fabrication of In_2O_3 nanostructures

Indium oxide (In_2O_3) nanostructures were synthesized at the ambient pressure through a modified chemical vapor deposition (CVD) system, as described previously [36–38]. A mixture of In_2O_3 and graphite powder with weight ratios 1:1.5 worked as the source and was loaded in the center of the furnace quartz tube. The n-Si (100) substrates ($1\text{--}10 \Omega\cdot\text{cm}$ resistivity, 0.5 mm thick, and $1 \times 1 \text{ cm}^2$) coated with a 10 nm gold film were positioned 1.5 cm downstream from the source to collect the products. Initially, the tube chamber was first pumped to a pressure below 20 millitorr to eliminate the air, and then the mixture of Ar (98%) and O₂ (2%) with a fixed gas flow of 100 sccm (standard cubic centimeters per minute) was introduced into the reaction chamber as carrying gas. During the fabrication of In_2O_3 nanowires, truncated octahedrons and octahedrons the furnace was heated up to 1100, 940 and 920 °C in about 70 min and kept at the respective temperature for 1 h. The preparations of In_2O_3 mixtures consisting of nanowires and nanoparticles were realized via the successive two-stage growth. In the first growth stage, the furnace was fixed at 1100 °C for 60 min. Subsequently, the furnace was lowered to 1000, 940 or 920 °C within 8 min and remained at each temperature for 30, 45 or 60 min, respectively. When the reactions were completed, the furnace was cooled down to room temperature naturally.

2.2. Materials characterization

The as-prepared In_2O_3 nanostructures were characterized by field-emission scanning electron microscopy (FE-SEM, Hitachi S4800) equipped with energy dispersive X-ray spectrometry (EDS), field-emission transmission electron microscopy (FE-TEM, JEOL-2100), X-ray powder diffractometry (XRD, Philips, Xpert), X-ray photoelectron spectroscopy (XPS, PHI5000 Versa Probe), VARIAN Cary5000 spectrophotometer, electron spin resonance spectrometer (EPR, A300-10/12, Bruker) and Edinburgh FLS-920 PL spectrometer.

2.3. KPFM and SRSPV characterization

Prior to the KPFM and SRSPV measurements, the In_2O_3 crystal facet-based homojunctions were firstly dispersed in ethanol by ultrasonic treatment and then deposited on ITO substrate by spin casting. The surface potential images of the sample were recorded by KPFM under ambient atmosphere conditions with an AM-KPFM mode. For the measurement of the surface potential, a lift mode was utilized with a lift height of 100 nm. In the lift mode, the topography and surface potential signals were sequentially acquired. In the first scan, the topography of the sample was obtained along a scan line. Then, a second scan was carried out along the first scan profile, recording the changes in the local surface potential. The Pt/Ir coated Si tip was employed as a Kelvin tip with a spring constant of $1\text{--}5 \text{ N m}^{-1}$ and resonant frequency of 60–100 kHz. To obtain the SPV, the tips were scanned in a very small region (about 10 nm) to average the signal while maintaining spatial resolution. During the measurement of the SPV, the illumination system with 500 W xenon-arc lamp, a Zolix Omni-λ 500 monochromator and a series of lenses was set up. To quantify the SPV, the varied surface potential signals were fed to Stanford SR 830 lock-in amplifier. The acquired R value together with the wavelength of the incident light was the SPV.

2.4. Facet-selective photo-deposition experiment

In a typical process, metal and metal oxide were simultaneously deposited on the different facets of the In_2O_3 crystal facet-based homojunction at room temperature without change in pH value. Specifically, 0.1 g In_2O_3 crystal facet-based homojunctions, 5 ml H_2AuCl_4 (0.005 mol/L), and 5 ml $\text{Co}(\text{NO}_3)_2$ (0.002 mol/L) solution were mixed in a vial. The mixture was then illuminated by a 300 W Xe lamp for 5 h. After photo-deposition, the products were isolated by centrifugation and washed with deionized water for several times, and then dried at 60 °C for overnight.

2.5. Computational method

We have employed the Vienna Ab Initio Package (VASP) to perform all the density functional theory (DFT) calculations within the generalized gradient approximation (GGA) using the PBE formulation. We have chosen the projected augmented wave (PAW) potentials to describe the ionic cores and take valence electrons into account using a plane wave basis set with a kinetic energy cutoff of 400 eV. Partial occupancies of the Kohn–Sham orbitals were allowed using the Gaussian smearing method and a width of 0.05 eV. The electronic energy was considered self-consistent when the energy change was smaller than 10^{-5} eV . A geometry optimization was considered convergent when the force change was smaller than $0.02 \text{ eV}/\text{\AA}$. Grimme's DFT-D3 methodology was used to describe the dispersion interactions.

The equilibrium lattice constant of cubic In_2O_3 unit cell was optimized, when using a $2 \times 2 \times 2$ Monkhorst-Pack k-point grid for Brillouin zone sampling, to be $a = 10.238 \text{ \AA}$. We then use it to construct two In_2O_3 surface models. One is a In_2O_3 (111) surface model with p (1×1) periodicity in the x and y directions and 2 stoichiometric layers in the z direction separated by a vacuum layer in the depth of 15 \AA in order to separate the surface slab from its periodic duplicates. This surface model

contains 64 In and 96 O atoms. During structural optimizations, the gamma point in the Brillouin zone was used for k-point sampling, and the bottom stoichiometric layer was fixed while the top one was allowed to relax. The other surface model is a In_2O_3 (001) surface model with p (1×1) periodicity in the x and y directions and 1 stoichiometric layer in the z direction separated by a vacuum layer in the depth of 15 Å in order to separate the surface slab from its periodic duplicates. This surface model contains 32 In and 48 O atoms. During structural optimizations, the gamma point in the Brillouin zone was used for k-point sampling, and the bottom half stoichiometric layer was fixed while the top half was allowed to relax.

2.6. Photoelectrochemical characterization

PEC measurements were conducted in a three-electrode system utilizing the epoxy-sealed In_2O_3 nanostructures with an exposed area of 0.5 cm^2 as the working electrode, Pt mesh as the counter electrode, Ag/AgCl (3 mol/L KCl-filled) as the reference electrode in 1 M NaOH (pH = 13.6) solution. The NaOH solution was purged with high purity N₂ (99.999%) for 1 h under vigorous stirring to remove the dissolved oxygen. The ohmic contacts were established on the backside of the Si substrate utilizing the eutectic gallium-indium alloy. The light source was the 500 W Xe lamp (Solar 500, NBet Group Corp.) with calibrated intensity of 100 mW/cm² and a water filter was used to reduce the infrared heating of the electrolyte. For the chemical and structural stability tests, the photocurrent versus time ($J-t$) curves were tested at 0.22

V vs. Ag/AgCl. The thermodynamic potential for oxygen evolution was calculated on basis of the Nernst equation: $E_0(\text{O}_2/\text{H}_2\text{O}) = 1.23 - 0.05917p\text{H} = 0.42V_{\text{NHE}} = 0.22V_{\text{AgCl}/\text{Ag}}$. The amounts of evolved oxygen were quantified by an Ocean Optics oxygen sensor system equipped with a FOXY probe (Neo-Fox Phase Measurement System), which was conducted together with chemical and structural stability tests.

3. Results and discussion

3.1. Fabrications and morphological characterizations of the In_2O_3 nanostructures

Our previous investigations found that the square In_2O_3 nanowires can be fabricated via the combined vapor-liquid-solid (VLS) and vapor solid (VS) mechanisms [37,38]. Fig. S1a and Fig. 1a-c depict the typical experimental parameters of the square In_2O_3 nanowires and the corresponding FE-SEM images. As can be seen, when the furnace tube was heated up to 1100 °C for 1 h, the square In_2O_3 nanowires with four smooth lateral facets were synthesized in a large scale. The average width of the square In_2O_3 nanowires is around 100 nm and their lengths are up to several hundreds of micrometers. XRD and FE-TEM characterizations verify that the as-prepared In_2O_3 nanowires grow along the [001] direction and are terminated by four {001} facets (Fig. S1b and Fig. S2). Additionally, we also demonstrated that the In_2O_3 nanoparticles can be produced through the vapor solid (VS) mechanism [36]. When the growth temperature was set to 920 °C keeping the other

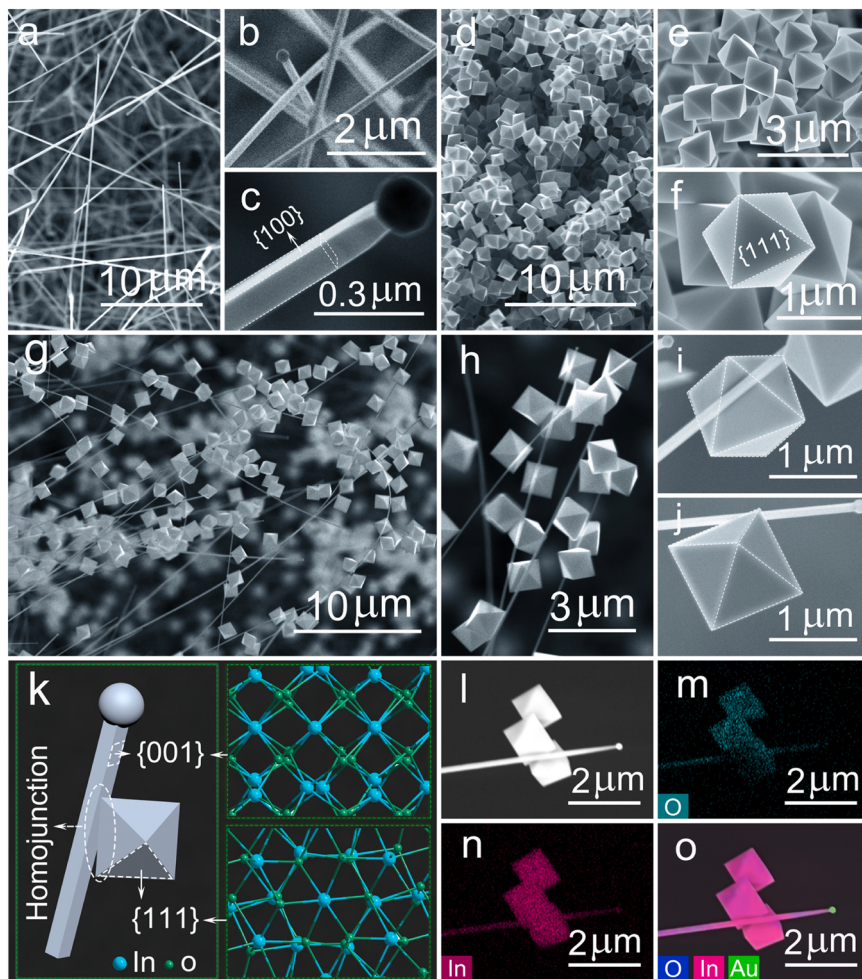


Fig. 1. (a-j) FE-SEM images of the as-synthesized In_2O_3 nanostructures with different magnifications: (a-c) In_2O_3 nanowires, (d-f) In_2O_3 octahedrons, (g-j) In_2O_3 crystal facet-based homojunctions. (k-o) Schematic diagram of the In_2O_3 crystal facet-based homojunctions and the corresponding EDX elemental mapping images indicating even elemental distribution of In and O, strong Au signal can be clearly observed at the tip of nanowire.

experimental parameters invariable (Fig. S3a), a large quantity of perfect In_2O_3 octahedrons with uniform edge size of around 1 μm was prepared (Fig. 1d-f). From the structural analysis, we can conclude that octahedrons are enclosed by eight triangular {111} facets (Fig. S3b and Fig. S4). These results clearly reflect that the morphologies of In_2O_3 nanostructures and growth behavior can be easily steered by adjusting the growth temperature during the CVD process. Hence, it is speculated that the epitaxial growth of the octahedrons on the lateral facets of nanowire would be realized when we carry out the successive two-stage CVD.

Fig. S5 displays the grow process including two stages. Stage I and II are designed to grow nanowires and epitaxial octahedrons, respectively. Between them is a transition period, in which the growth temperature is abruptly dropped from 1100 to 920 °C. The abrupt dropping of the growth temperature dramatically reduces the gas-phase supersaturation of In_2O_3 [36]. This can effectively switch the growth mechanism of nanostructures from the combined VLS and VS to the single VS, which will be discussed later in more detail. Fig. 1g-j and Fig. S6 are the typical FE-SEM images of the innovative In_2O_3 crystal facet-based homojunctions, revealing that a significant number of epitaxial octahedrons are randomly distributed on the lateral facets of long nanowires resembling a long chain of octahedral beads. Both the octahedrons and nanowires of homojunctions show no evident difference in the size compared with those of the standalone ones. From the magnified FE-SEM images (Fig. 1h-j), intimate contacts between the octahedrons and square nanowires can be observed clearly, indicating that octahedrons are epitaxially grown on the lateral facets of nanowires, which is described by the 3D representation in Fig. 1k. Moreover, the number of epitaxial octahedrons increases gradually with the duration of the growth stage II increasing from 30 to 45 and 60 min (Fig. S7), and the corresponding samples are referred to homojunctions 1, homojunctions 2 and homojunctions 3.

The influence of temperature on the growth stage II was also systematically investigated. When the temperature of the growth stage II was lowered to 1000 °C, while the experimental parameters of the growth stage I were kept constant, the growth of the epitaxial nanoparticles follow the VS mechanism, and they display cubic morphologies, similar to standalone cubes that were fabricated previously

(Fig. S8) [36]. The magnified FE-SEM image shows that the cube is enclosed by six square {001} facets (Fig. S8c, referred to cube-nanowire mixtures). With further reducing the temperature of the growth stage II to 940 °C, the epitaxial nanoparticles present truncated octahedral shapes with six square {001} and eight hexagonal {111} facets (Fig. S9, referred to truncated-octahedron-nanowire mixtures). These results demonstrate that the temperature of the growth stage II plays a decisive role in the morphology evolution of the epitaxial nanoparticles from cube to truncated octahedron and finally octahedron.

3.2. Growth mechanism of the In_2O_3 nanostructures

To unveil the growth mechanism of the as-prepared In_2O_3 nanostructures, the time-dependent morphological evolution was characterized by FE-SEM, and the results are presented in Fig. 2. The whole growth process can be divided into two sequential stages, namely the growth of nanowires and epitaxial nanoparticles. In principle, the VLS growth requires a higher gas-supersaturation than the VS growth since the former consumes more vapor growth species [44]. As a result, under the relatively high gas-supersaturation because of the relatively high growth temperature of 1100 °C, the growth of the square In_2O_3 nanowires can be interpreted by the combined VLS and VS mechanism. In the beginning, the Au nanodroplets firstly form owing to the splitting of Au film over the Si substrate, which subsequently act as the preferentially absorbed sites for the vapor In_2O_3 species (Fig. 2a and Fig. S10a). Then, Au-In alloy nanodroplets can be formed through alloying reaction between the Au nanodroplets and indium vapor produced by the carbo-thermal reduction of In_2O_3 powder [45,46]. With the continuous dissolution of the vapor In_2O_3 species into the Au-In alloy nanodroplets, the nanodroplets become supersaturated and the cylindrical nanowires start to grow via VLS mechanism (Fig. 2b and Fig. S10 b-g). As the growth continues, the absorbed In_2O_3 species would be transferred to the Au-In interface to maintain the one-dimensional (1D) longitudinal growth by the VLS mechanism [37,38]. As is well-known, the cylindrical nanowires are not stable because their surfaces contain high-index facets with large surface energy. To minimize the surface energy, some of the absorbed In_2O_3 species directly from vapor would simultaneously incorporate onto the lateral surface under the VS mechanism, resulting

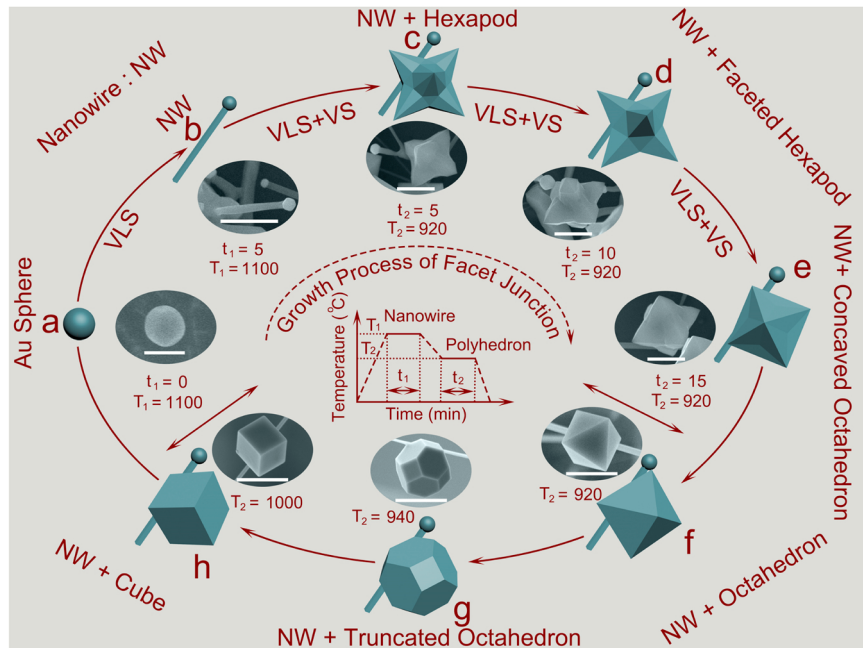


Fig. 2. Growth process of the In_2O_3 crystal facet-based homojunction and morphological evolution of the epitaxial nanoparticles. Scale bar: (a-b) 100 nm, (c-e) 500 nm, (f-h) 1 μm .

in the appearance of low-index crystal facets [37,38]. For the bcc In_2O_3 , the sequence of surface energy (γ) for low-index crystal facets is given as $\gamma_{\{111\}} < \gamma_{\{001\}} < \gamma_{\{110\}}$, and the growth rates of the corresponding facets follow the same sequence [47,48]. Furthermore, previous investigations have proved that the sequence of growth rates can be altered by adjusting the gas-supersaturation closely related to the growth temperature during the CVD process [36]. That is to say, the high supersaturation leads to the exposure of more high-energy facets owing to the conversion of energy [36,49]. At 1100 °C, the gas-supersaturation of the In_2O_3 species is relatively high to allow the appearance of {001} facets with higher surface energy, but not enough to produce the {110} facets with the highest surface energy. Accordingly, the square nanowires with four {001} facets can be formed under the relatively high gas-supersaturation of In_2O_3 [37,38,49].

In the second stage, the gas-supersaturation of the In_2O_3 vapor species reduces gradually with the growth temperature, and the supply of the In_2O_3 vapor species is insufficient to maintain the 1D growth. Under this circumstance, the 1D growth stops and new zero-dimensional (0D) nucleation and growth start from the lateral facets of the nanowires through the single VS mechanism. This is exemplified by the growth evolution of epitaxial In_2O_3 octahedrons (Fig. 2c-e). At the initial stage of second growth, the hexapod-like In_2O_3 nanostructures are epitaxially grown on the lateral facets of the nanowires (Fig. 2c). As the growth proceeds, more newly arriving In_2O_3 species would be absorbed on the surface of the hexapod-like In_2O_3 nanostructures. They are integrated into the crystal lattice along the $<001>$ direction and lead to the

appearance of {111} facets on top of the six pods (Fig. 2d, e). Prolonging the growth time of the stage II to 15 min, the epitaxial concaved In_2O_3 octahedrons turn into perfect octahedrons (Fig. 2f). The observation indicates that the gas-supersaturation of growth species can effectively switch the growth mechanism from combined VLS and VS to single VS. Besides, the morphologies of epitaxial In_2O_3 nanoparticles also depend on gas-supersaturation of In_2O_3 species. As the growth temperature of the growth stage II is reduced from 1000 to 920 °C, the epitaxial In_2O_3 nanoparticles vary from cube with {001} facets to truncated octahedron with both {111} and {001} facets, and finally to octahedron with {111} facets (Fig. 2g, h). This is because the high growth temperature leads to the high gas-supersaturation, and results in the formation of {001} facets with the higher surface energy, while the lower growth temperature leads to the lower gas-supersaturation, and facilitates the formation of the {111} facets with lower surface energy [36,49].

3.3. Structural and compositional characterization of the In_2O_3 nanostructures

The crystalline structures and compositions of the as-synthesized In_2O_3 nanostructures were checked by XRD and EDX. As depicted in Fig. S11, all the diffractions peaks could be indexed to the cubic In_2O_3 crystal (JCPDS Card, No.06–0416) [50]. However, it is worth noting that the diffraction intensity ratio of (222) to (400) of the homojunctions 2 is about 1.21, which is much higher than that of the nanowires (0.94) and much lower than that of the octahedrons (5.86). This means that the

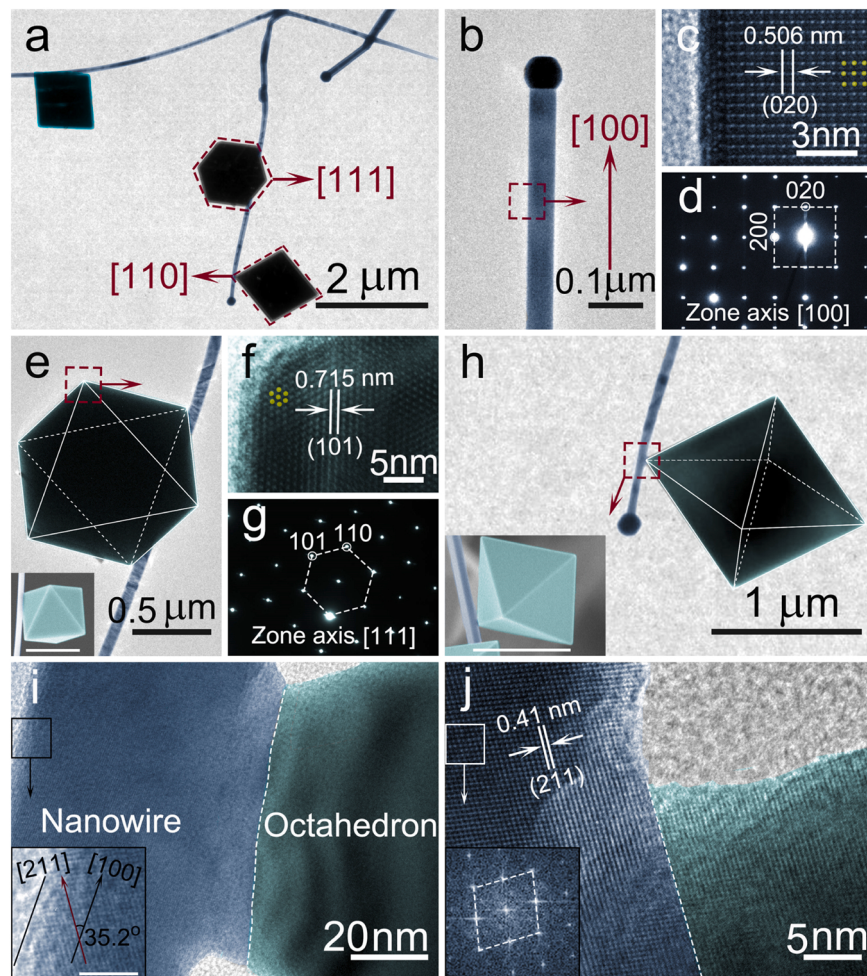


Fig. 3. (a, b, e, h) FE-TEM images of the In_2O_3 crystal facet-based homojunctions with different magnifications (Insets in (e) and (h) are the corresponding FE-SEM images viewed along [111] and [110] direction, respectively. Scale bars of Inset in (e) and (h): 1 μm . (c-d, f-g) HRTEM images and SAED patterns derived from red dashed box in the (b) and (e), respectively. (i-j) HRTEM images of the interface between In_2O_3 nanowire and the octahedron. Scale bars of Inset in (i): 5 nm.

homojunctions contain {111} and {001} facets, which is in consistent with the FE-SEM and FE-TEM results. The combined elemental mapping images display the spatial distribution of In, O, and Au (Fig. 1i-o), which reveals the formation of pure In_2O_3 product. The EDS spectra show that the In:O atomic ratio of nanowires, homojunctions 2 and octahedrons are distinct, and the corresponding values are 44.4:55.6, 45.3:54.7, 47.8:52.8, respectively. This implies that the morphological evolution of In_2O_3 have effect on the oxygen vacancies concentrations (Fig. S12).

Further microstructural characterizations were examined by FE-TEM. The low-resolution FE-TEM image shows that the surfaces of In_2O_3 nanowires are sporadically coated with In_2O_3 octahedrons with hexagonal and tetragonal projected shapes taken by focusing the electron beam parallel to [111] and [110] direction, respectively (Fig. 3a). The high-resolution FE-TEM (HRTEM) images and their selected area electron diffraction (SAED) patterns of the nanowire and octahedron of the homojunction are identical to those of standalone ones (Fig. 3b-g, Fig. S2 and Fig. S4). The HRTEM images of the interface region between the octahedron and nanowire marked with a red dashed box in Fig. 3 h and Fig. S13a, c show that lattice fringes nicely extend from the basal facet of nanowire to octahedron, attesting that octahedron nucleates on the lateral facets of nanowire and subsequently grows out of it (Fig. 3i, j and Fig. S13b, d). The HRTEM image and the fast Fourier transform diffraction pattern also show the lattice fringe of 0.41 nm, consistent with the lattice fringe of the (211) plane of cubic In_2O_3 (Fig. 3j). The angle between the (211) plane and left edge is 35.2°, which agrees well with the angle of (211) and (100) planes (Fig. 3i). Hence, it can be inferred that the nanowires grow along the [100] direction and are terminated by four {001} facets. Those results further illustrate that epitaxial octahedrons have intimate contacts with the nanowires. The continuous interfacial lattice fringes can serve as convenient and fast channels for the photogenerated charges transfer between two segments of the crystal facet-based homojunction.

3.4. Direct experimental evidence for the formation of crystal facet-based homojunction

KPFM and SRSPV techniques could directly image the local work

function and surface distribution of the photogenerated charges of semiconductor photocatalysts with nanometer scale spatial resolution and millivolt sensitivity [24,51–53]. The schematic diagram of the KPFM system including the SRSPV is illustrated in Fig. 4a. The AFM topography image shown in Fig. 4b reveals that the In_2O_3 crystal facet-based homojunction consists of nanowire and octahedron, which is in accordance with the FE-SEM and FE-TEM results. The corresponding KPFM image obtained in the dark is displayed in Fig. 4c. It is clear that the {001} facets are brighter on the color scale than the {111} facets, suggesting that the surface potential of the former is higher than that of the latter [24]. This result is also testified by the contact potential difference (CPD) distribution extracted across the dashed line in Fig. 4c and Fig. S14a, which shows that the surface potential of {001} facets is approximately 30 mV higher than that of the {111} facets (Fig. S14b). The surface potential is defined as CPD between the sample surface and the Kelvin tip ($\text{CPD} = (\Phi_{\text{tip}} - \Phi_{\text{surface}})/e$, where Φ_{tip} and Φ_{surface} represent the work functions of the Kelvin tip and the sample surface, and e is the electronic charge) [52,54]. As a result, it can be derived that the work function of the {001} facet is lower than that of the {111} facets, which can create the oriented built-in electric field from {111} to {001} facets across the nanowire/octahedron interface and expedite the separation of the photogenerated charges. The work function difference between {001} and {111} facets also show the difference in the surface band bending. Upon irradiation, the corresponding KPFM image becomes brighter suggesting increased surface potential (Fig. 4d, Fig. S14b, c). The variation in surface potential unambiguously reflects that there are conspicuous changes of charge balance in the space charge regions (SCRs) beneath the two facets, which suggests that the two facets exhibit upward band bending in the SCRs [24].

Fig. 4e presents the SRSPV measured on two surface spots of the In_2O_3 crystal facet-based homojunction (Fig. 4b), one on the {001} facets (P_1) and another on the {111} facets (P_2). Both of the two facets display a SPV response at photoexcitation energy larger than 2.8 eV that corresponds to bandgap of the In_2O_3 , showing that SPV results are induced by the band-to-band transition of In_2O_3 . The amplitude of SPV signal of {001} facets is much higher than that of the {111} facets. More specifically, the SPV signal of {001} facets obtained at 3.3 eV is 2.7

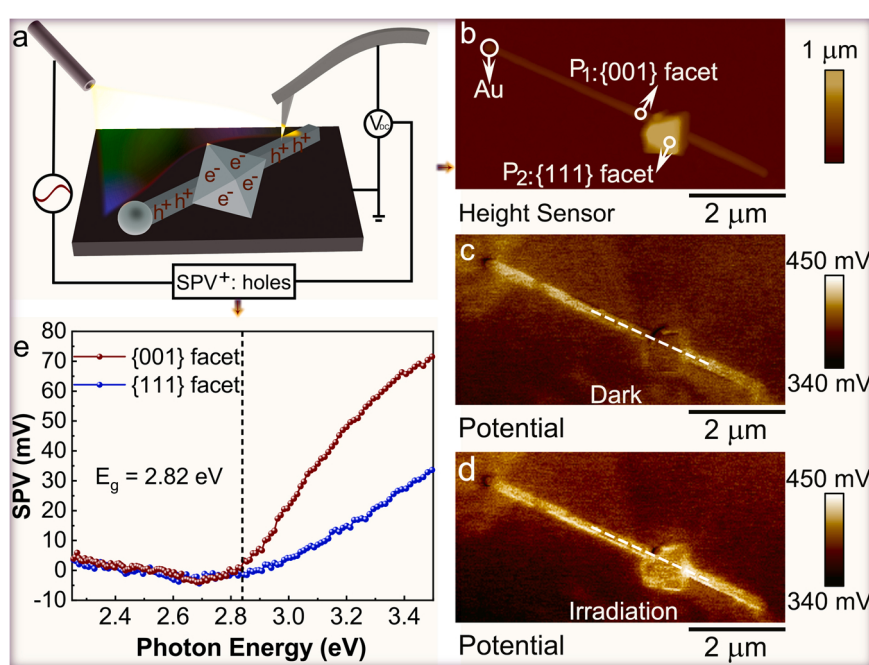


Fig. 4. (a) Schematic diagram of the KPFM systems to obtain the energy band alignment of the In_2O_3 crystal facet-based homojunction. (b) AFM topography image of the single In_2O_3 crystal facet-based homojunction on ITO substrate. (c, d) Corresponding KPFM images obtained in the dark and under irradiation with 400 nm light. (e) Spatially resolved SPV spectra measured on {001} facets, P_1 and {111} facets, P_2 on a single In_2O_3 crystal facet-based homojunction.

times higher than that of the {111} facets, suggesting the hole-accumulating capacity of {001} facets is stronger than that of the {111} facets, making the photogenerated holes preferably accumulate on the {001} facets, and vice versa. Similar phenomena have been confirmed for other single polyhedral photocatalyst particles with co-exposed different facets [10,12,24,51–55].

To further prove the above distribution of the photogenerated charges, *in situ* photochemical reduction and oxidation probing reactions were carried out in HAuCl₄ and Co(NO₃)₂ solution. Fig. S15a, b are the low-magnification FE-TEM images of the In₂O₃ crystal facet-based homojunction before and after the *in situ* photo-depositions of Au and Co₃O₄. It can be observed that the surface of the In₂O₃ crystal facet-based homojunction become rough after the *in situ* photo-depositions, demonstrating that the Co₃O₄ and Au nanoparticles are selectively deposited on the surface of the nanowire and octahedron, respectively. This is also confirmed by the HRTEM image from the surface of the nanowire, in which the well-resolved lattice fringe of 0.46 nm well matches with the (111) plane of Co₃O₄ (Fig. S15c). While the Au nanoparticles only sit on the surface of the octahedron rather than on the nanowire, as evidenced by the lattice fringe of 0.24 nm belonging to the (111) plane of Au (Fig. S15d). These observations uncover that the photogenerated electrons tend to accumulate on the {111} facets to trigger the reductive reaction ($Au^{3+} + 3e^- \rightarrow Au$), and the photogenerated holes are preferable for migrating to the {001} facets to participate in oxidation reaction ($3Co^{2+} + 4H_2O + 6h^+ \rightarrow Co_3O_4 + 8H^+$). The *in situ* photo-deposition results are well consistent with those obtained from the above KPFM and SRSPV, both of which provide direct evidences for the aforementioned conclusions that a built-in electric field from {111} to {001} facets across the nanowire/octahedron interface is formed. Under the driving of oriented build-in electric field, photogenerated electrons and holes are separated toward the surfaces of octahedrons and nanowires, respectively.

3.5. DFT calculations

DFT calculations were also implemented to acquire the further

insights into the separation mechanism of photogenerated charges and the nature of band bending of the In₂O₃ homojunction. The electronic structures and work functions of exposed facets are determined by their atomic arrangements and coordination [17,22,28,31]. From the viewpoint of stacking sequence, the In and O atoms are alternatively arranged to form the outermost structures on the {001} facet but mixed on the {111} facet (Fig. 1 K). Considering the atomic arrangements, the {001} facet is highly polar, whereas the {111} is nonpolar. Undoubtedly, the intrinsic variation in surface atomic arrangements is capable of inducing different surface electronic structures and work functions. As displayed in Fig. 5, the density of states for In₂O₃ {001} and {111} facets unveil that the valence band maximum (VBM) mainly originates from the O 2p orbital, whereas the conduction band minimum (CBM) is dominated by the In 5 s orbital (Fig. 5a). More importantly, the calculation results also show that the VBM and CBM positions of {001} facet are more positive than those of {111} facet, and the work function of {001} (ca. 4.8 eV) is lower than that of the {111} facet (ca. 5.38 eV) (Fig. 5a, b). The differences of the band positions and work functions between the two facets result in the formation of oriented build-in electric field from {111} to {001} facets across the nanowire/octahedron interface. Given that the Fermi level position of bulk In₂O₃, an n-type semiconductor, is near the CBM, it has upward surface band bending for thermodynamic equilibrium. The surface band bending of the {001} facet is obviously than that of the {111} facet on account of its positive band positions and low work function. Based on the above results, we can obtain the band diagram of the In₂O₃ crystal facet-based homojunction as depicted in Fig. 5c. Therefore, under the driving of oriented built-in electric field owing to work function difference, photogenerated electrons prefer to accumulate on the {111} facets and the photogenerated holes tend to gather on the {001} facets (Fig. 5c). In addition, the partial charge density map of the CBM electronic state of the {111} facets possess better orientations of In 5 s orbitals than that of {001} facets, rendering electron transfer toward {111} facets much more easier than {001} facets. Meanwhile, the partial charge density map of the VBM electronics states of {001} facets is delocalized over O 2p throughout the crystal lattice, while that of {111}

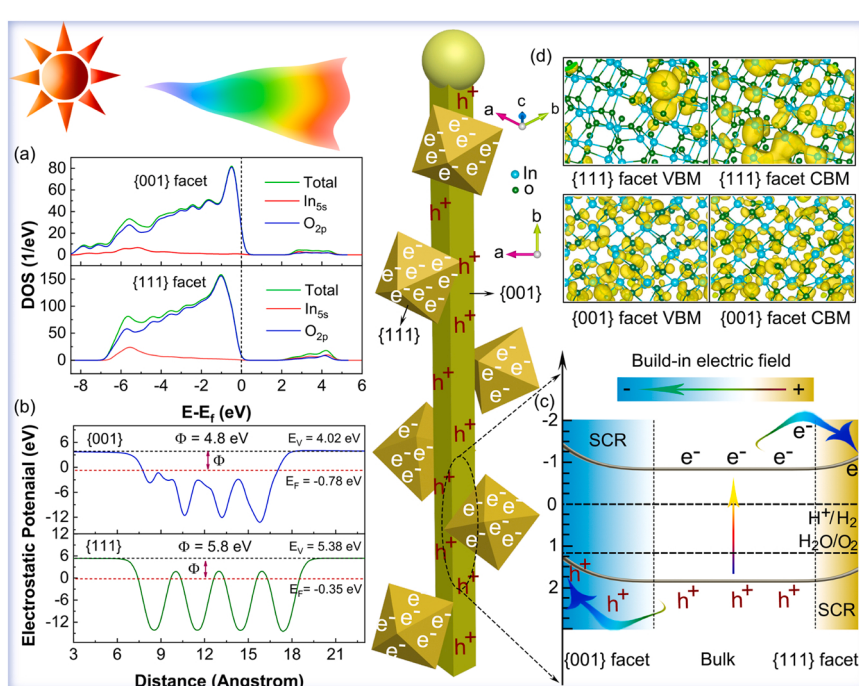


Fig. 5. (a) Densities of states of {001} and {111} facets. (b) Electrostatic potential profiles for the {001} and {111} facets. (c) Schematic illustration of photogenerated charges separation induced by the oriented build-in field from {111} to {001} facets of the In₂O₃ homojunctions. (d) Partial charge density maps for VBM and CBM of the {001} and {111} facets.

facets is located on some O 2p orbitals, which demonstrates that photogenerated holes are more prone to migrate to {001} facets (Fig. 5d) [56]. These results are in good accordance with our KPFM, SRSPV and in situ photo-deposition results.

3.6. PEC performances of the In_2O_3 nanostructures

The PEC water splitting activities were evaluated using the as-synthesized In_2O_3 nanostructures as photoanodes. As shown in Fig. 6a, all the samples display the negligible dark currents with respect to their photocurrents. Under irradiation, the photocurrent densities collected from the homojunctions steeply rise and largely surpass those of the standalone nanowires and octahedrons in the entire potential range of -0.6 – 0.6 V vs. Ag/AgCl, suggesting the higher PEC activity of the

homojunctions. In addition, the photocurrent density of homojunction increases with an increasing duration of the growth stage II from 30 to 45 min, but decreases if the duration further increases to 60 min. This is because the duration of the growth stage II of 60 min leads to the excessive abundance of the epitaxial octahedrons, which may reduce the number of the active sites on {001} facets. To demonstrate this trend more clearly, the chronoamperometry measurements were performed under illumination with several 10 s light on/off cycles at 0.22 V vs. Ag/AgCl [1.23 V vs. RHE (reversible hydrogen electrode)] (Fig. 6b). Obviously, all the In_2O_3 samples show the rapid and reproducible photocurrent responses upon each cycle irradiation, which implies that the observed photocurrents derive from the light irradiation. At the 0.22 V vs. Ag/AgCl, the homojunctions 2 with moderate number of epitaxial octahedrons yields the maximal photocurrent density of 1.42 mA/cm^2 , which is about 7.1 and 28.4 times those of standalone nanowires and octahedrons, respectively. The low photocurrent densities of the standalone nanowires and octahedrons can be attributed to the fact that the photogenerated electrons and holes could not be spatially separated on the single crystal facet [39,57]. Previous reports have suggested that the Au nanodroplets at the tip of nanowires could promote the separation of the photogenerated charges, and thus enhance the PEC performance [38,58]. However, in this work, the contact areas between In_2O_3 nanowires and apical Au nanodroplets are far less than the lateral areas of In_2O_3 nanowires and crystal facet-based homojunctions because of their lengths of several hundreds of micrometers. As a consequence, apical Au nanodroplets play a minor role in the PEC performance of the In_2O_3 nanowires and crystal facet-based homojunctions.

To underline the advantage of this kind of crystal facet-based homojunction, we also fabricated standalone In_2O_3 truncated octahedrons, namely, traditional crystal facet-based homojunction, for comparison. It was found that each truncated octahedron possesses the six square {001} and eight hexagonal {111} facets (Fig. S16a, b). Although the truncated octahedrons yield a higher current density (0.4 mA/cm^2) as compared to nanowires and octahedrons, it is still much lower than the homojunctions 2 (Fig. S16c-e). The result implies that the photogenerated charges separation of the In_2O_3 homojunctions consisting of nanowire exclusively enclosed by {001} facets and octahedron fully surrounded by {111} facets are more effective than those of the truncated octahedron owing to its long spatial distance (Fig. S16c-e). Moreover, this minimum photocurrent density of the homojunction 1 (0.8 mA/cm^2) is also higher than those of truncated-octahedron-nanowire mixtures (0.65 mA/cm^2), cube-nanowire mixtures (0.5 mA/cm^2), manifesting the superiority of homojunctions for boosting PEC water splitting (Fig. S17).

Photostability and Faradaic efficiency are two important evaluations for the practical application of photoanodes. Fig. 6c displays the photocurrent-time ($J-t$) curves of the In_2O_3 nanostructures measured at 0.22 V vs. Ag/AgCl under illumination. Both the homojunction 2 and nanowires exhibit no discernable deterioration in the photocurrent density over 180 min. The amount of evolved oxygen increases linearly with the test time with unit Faraday efficiency. Moreover, there is no significant changes in the surface morphology and crystal phase before and after PEC water splitting for 180 min (Fig. S18). These results elucidate an excellent stability of homojunction during the PEC water splitting process.

To identify the origin of enhanced photocurrent, UV-vis, XPS and EPR were examined. UV-vis diffuse reflectance spectra in the Fig. S19 illustrate that the absorption edges of the standalone nanowires, homojunction 2 and standalone octahedrons have slight differences, and the corresponding bandgap are calculated to be approximately 2.88, 2.82, and 2.78 eV, respectively. Theoretically, a smaller bandgap usually leads to a larger photocurrent density. However, in the present case, the photocurrent density of the standalone octahedrons is much lower than those of standalone nanowires and homojunctions 2, unraveling that the contribution of the bandgap shrinkage is quite limited. The PEC water splitting activity can also be affected by the oxygen vacancies

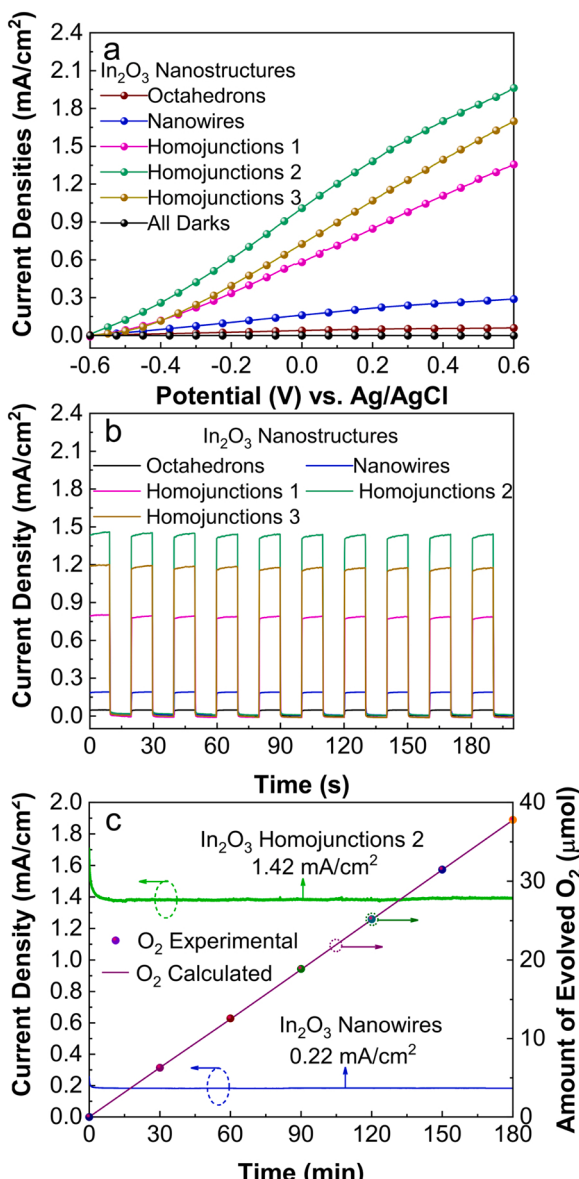


Fig. 6. (a) Current versus voltage (J - V) curves collected from the In_2O_3 nanowires, octahedron and crystal facet-based homojunctions. (b) Corresponding transient photocurrent responses performed at 0.22 V vs. Ag/AgCl. (c) Photocurrent versus time (J - t) curves of In_2O_3 nanowires and crystal facet-based homojunctions 2 obtained at 0.22 V vs. Ag/AgCl. The solid line and colorful spheres represent the amount of evolved O_2 calculated theoretically and detected experimentally of the In_2O_3 crystal facet-based homojunctions 2, respectively.

concentrations of the samples. The XPS and EPR results reveals that the octahedrons possess the highest oxygen vacancies concentrations, while the other two samples exhibit the relative smaller oxygen vacancies concentrations (Fig. S20), which is in agreement with EDS results [59, 60]. Assuming oxygen vacancies play a dominant role, the octahedrons should have the largest photocurrent, but our experimental results are not so. The above results solidify that the superior PEC activity of the homojunction 2 is ascribed to the accelerated separations, transfers and surface reactions of the photogenerated charges induced by the unique homojunction structure, rather than the variation of both absorption properties and oxygen vacancies concentrations. This is further evidenced by their photoluminescence (PL) emission (Fig. S21a) stemming from the radiative recombination of free charge [31,61,62]. The intensity of PL emission peak of homojunctions 2 is lower than those of the nanowires, octahedrons and truncated octahedrons, illustrating that it has the higher capability of suppressing the charge carrier recombination. The electrochemical impedance spectroscopy data further demonstrates that the radius of the homojunction 2 is the smallest among the four samples under light irradiation (Fig. S21b), which attests that more effective separation of photogenerated charges and faster interfacial charge transfer occurred in the homojunctions 2.

4. Conclusion

In summary, the innovative In_2O_3 crystal facet-based homojunctions comprising of square nanowires exclusively enclosed by $\{001\}$ facets and octahedrons fully surrounded by $\{111\}$ facets were synthesized on a large scale through the successive two-stage CVD. The growth mechanism during the CVD were systematically explored, and the new understanding enables delicate control over the exposure of crystal facet. Additionally, the KPFM, SRSPV and facet-selective photo-depositions provide the direct evidence for the accumulation of photogenerated electrons and holes on the surface of the epitaxial octahedrons and nanowires, respectively, achieving the effective charges separation with long spatial distances. The theoretical calculations clearly demonstrated that the oriented build-in electric field caused by surface work function difference or band bending difference of the $\{111\}$ and $\{001\}$ facets is the main driving force for the charges separation. In addition, the well-matched lattice fringes between the In_2O_3 epitaxial octahedrons and nanowires serve as the convenient and fast channels for the charge transfer between two sections of homojunctions, further accelerating the charges separation. Benefiting from these advantages, the innovative In_2O_3 crystal facet-based homojunctions grown at optimal condition delivered a photocurrent density of $1.42 \text{ mA}/\text{cm}^2$ at 0.22 V vs. Ag/AgCl , nearly 7.1 and 28.4 times those of standalone nanowires and octahedrons, respectively. This value is also higher than that of the In_2O_3 truncated octahedrons ($0.4 \text{ mA}/\text{cm}^2$), namely, traditional crystal facet-based homojunctions. These outcomes pave a new avenue towards design and exploitation of the facet-oriented photoelectrodes for other applications such as photodetectors, solar cells and photocatalysis.

CRediT authorship contribution statement

The work was conceived and designed by Ming Meng, Lizhe Liu, and Jun Li. Liwei Wang and Chunyang Li accomplished the experiments, wrote the manuscript. Yuanyuan Chen assisted to accomplish the experiments and revise the manuscript. Kun Xu and Jitao Li finished the FE-SEM and FE-TEM characterization and analysis. Honglei Yuan carried out the photoelectrochemical tests. Zhixing Gan provided resource, conceived the study and revised the manuscript. All the authors discussed the results.

Declaration of Competing Interest

The authors declare that they have no known competing financial interests or personal relationships that could have appeared to influence

the work reported in this paper.

Acknowledgments

This work was supported by National Natural Science Foundation of China (12174183, 51702379), Natural Science Foundation of Henan Province (222300420597), Science and Technology Project of Henan Province (212102210536, 22B120006), Taishan Scholars Program of Shandong Province (tsqn201909117), China Postdoctoral Science Foundation (2020TQ0277, 2020M682328), Postdoctoral Science Foundation of Henan Province (202002010). The DFT calculation is supported by Supercomputer Center in Zhengzhou University (Zhengzhou).

Appendix A. Supporting Information

Schematic illustration of the dynamic temperature profiles used in the preparation of In_2O_3 crystal facet-based homojunctions, nanowires, octahedron. Cross-sections of the surface potential images of a single In_2O_3 crystal facet-based homojunction. FE-TEM images of a single In_2O_3 crystal facet-based homojunction before and after the in situ photo-deposition of Au and Co_3O_4 . FE-SEM images, EDS spectra, FE-TEM images, XRD patterns, UV-vis absorption spectra, XPS spectra, EPR spectra, Room-temperature photoluminescence spectra, Electrochemical impedance spectra and In_2O_3 crystal facet-based homojunctions, nanowires, octahedron. FE-SEM images, EDS spectra and current versus voltage ($J-V$) curves of the In_2O_3 truncated-octahedron-nanowire mixtures, cube-nanowire mixtures, truncated octahedron and the corresponding transient photocurrent responses performed at 0.22 V vs. Ag/AgCl .

Appendix B. Supporting information

Supplementary data associated with this article can be found in the online version at doi:10.1016/j.apcatb.2022.122071.

References

- [1] B.B. Zhang, S.Q. Yu, Y. Dai, X.J. Huang, L.J. Chou, G.X. Lu, G.J. Dong, Y.P. Bi, Nitrogen-incorporation activates NiFeO_x catalysts for efficiently boosting oxygen evolution activity and stability of BiVO_4 photoanodes, *Nat. Commun.* 12 (2021) 6969.
- [2] X.M. Zhang, P.L. Zhai, Y.X. Zhang, Y.Z. Wu, C. Wang, L. Ran, J.F. Gao, Z.W. Li, B. Zhang, Z.Z. Fan, L.C. Sun, J.G. Hou, Engineering single-atomic $\text{Ni-N}_4\text{-O}$ sites on semiconductor photoanodes for high-performance photoelectrochemical water splitting, *J. Am. Chem. Soc.* 143 (2021) 20657–20669.
- [3] S.J. Liu, R.T. Gao, R.G. Zhang, Z.W. Wang, X.H. Liu, T. Nakajima, X.Y. Zhang, Y. G. Su, L. Wang, Tungsten induced defects control on BiVO_4 photoanodes for enhanced solar water splitting performance and photocorrosion resistance, *Appl. Catal. B Environ.* 298 (2021), 120610.
- [4] M.R. Nellist, F.A.L. Laskowski, J.J. Qiu, H. Hajibabaei, K. Sivula, T.W. Hamann, S. W. Boettcher, Potential-sensing electrochemical atomic force microscopy for in operando analysis of water splitting catalysts and interfaces, *Nat. Mater.* 19 (2020) 69–76.
- [5] Y. Li, Q. Mei, Z.J. Liu, X.S. Hu, Z.H. Zhou, J.W. Huang, B. Bai, H. Liu, F. Ding, Q. Z. Wang, Fluorine-doped iron oxyhydroxide cocatalyst: promotion on the WO_3 photoanode conducted photoelectrochemical water splitting, *Appl. Catal. B Environ.* 304 (2022), 120995.
- [6] V. Nandal, Y. Pihosh, T. Higashi, T. Minegishi, T. Yamad, K. Seki, M. Sugiyamad, K. Domen, Probing fundamental losses in nanostructured Ta_2N_5 photoanodes: design principles for efficient water oxidation, *Energy Environ. Sci.* 14 (2021) 4037–4047.
- [7] H.M. Wang, Y.G. Xia, N. Wen, Z. Shu, X.L. Jiao, D.R. Chen, Surface states regulation of sulfide-based photoanode for photoelectrochemical water splitting, *Appl. Catal. B: Environ.* 300 (2022), 120717.
- [8] P. Reddy Narangari, J.D. Butson, H.H. Tan, C. Jagadish, S. Karuturi, Surface-tailored InP nanowires via self-assembled Au nanodots for efficient and stable photoelectrochemical hydrogen evolution, *Nano Lett.* 21 (2021) 6967–6974.
- [9] W.Y. Jiang, Y. An, Z.Y. Wang, M.R. Wang, X.L. Bao, L.R. Zheng, H.F. Cheng, P. Wang, Y.Y. Liu, Z.K. Zheng, Y. Dai, B.B. Huang, Stress-induced BiVO_4 photoanode for enhanced photoelectrochemical performance, *Appl. Catal. B Environ.* 304 (2022), 121012.

- [10] R.T. Chen, S. Pang, H.Y. An, J. Zhu, S. Ye, Y.Y. Gao, F.T. Fan, C. Li, Charge separation via asymmetric illumination in photocatalytic Cu₂O particles, *Nat. Mater.* 3 (2018) 655–663.
- [11] W.R. Wang, B.D. Guo, H.T. Dai, C. Zhao, G.C. Xie, R.P. Ma, M.Z. Akram, H.Y. Shan, C.Z. Cai, Z.Y. Fang, J.R. Gong, Improving the water oxidation efficiency with a light-induced electric field in nanograting photoanodes, *Nano Lett.* 19 (2019) 6133–6139.
- [12] R.G. Li, F.X. Zhang, D.E. Wang, J.X. Yang, M.R. Li, J. Zhu, X. Zhou, H.X. Han, C. Li, Spatial separation of photogenerated electrons and holes among {010} and {110} crystal facets of BiVO₄, *Nat. Commun.* 4 (2012) 1432.
- [13] T.C. Wei, Y.N. Zhu, Z.N. Gu, X.Q. An, L.M. Liu, Y.X. Wu, H.J. Liu, J.W. Tang, J. H. Qu, Multi-electric field modulation for photocatalytic oxygen evolution: enhanced charge separation by coupling oxygen vacancies with faceted heterostructures, *Nano Energy* 51 (2018) 764–773.
- [14] D. Li, Y. Liu, W.W. Shi, C.Y. Shao, S.Y. Wang, C.M. Ding, T.F. Liu, F.T. Fan, J.Y. Shi, C. Li, Crystallographic-orientation-dependent charge separation of BiVO₄ for solar water oxidation, *ACS Energy Lett.* 4 (2019) 825–831.
- [15] Y.L. Li, Q. Zhao, Y. Zhang, Y.C. Li, L.Z. Fan, F.T. Li, X.H. Li, In-situ construction of sequential heterostructured CoS/CdS/CuS for building “electron-welcome zone” to enhance solar-to-hydrogen conversion, *Appl. Catal. B Environ.* 300 (2021), 120763.
- [16] X. Wang, Q. Xu, M.R. Li, S. Shen, X.L. Wang, Y.C. Wang, Z.C. Feng, J.Y. Shi, H. X. Han, Can Li, Photocatalytic overall water splitting promoted by an α -phase Junction on Ga₂O₃, *Angew. Chem. Int.* 51 (2012) 13089–13092.
- [17] S.C. Wang, G. Liu, L.Z. Wang, Crystal facet engineering of photoelectrodes for photoelectrochemical water splitting, *Chem. Rev.* 119 (2019) 5192–5247.
- [18] D. Yin, X.M. Ning, P.Y. Du, D.X. Zhang, Q. Zhang, X.Q. Lu, Cascaded multiple-step hole transfer for enhancing photoelectrochemical water splitting, *Appl. Catal. B Environ.* 296 (2021), 120313.
- [19] E. Samuel, B. Joshi, M.W. Kim, M.T. Swihart, S.S. Yoon, Morphology engineering of photoelectrodes for efficient photoelectrochemical water splitting, *Nano Energy* 72 (2020), 104648.
- [20] C.Q. Cheng, G.H. Liu, K. Du, G. Li, W.D. Zhang, S. Sanna, Y.Z. Chen, N. Pryds, K. Y. Wang, Enhanced visible light catalytic activity of MoS₂/TiO₂/Ti photocathode by hybrid-junction, *Appl. Catal. B Environ.* 237 (2018) 416–423.
- [21] N. Wei, Y. Liu, M. Feng, Z.X. Li, S.G. Chen, Y.B. Zheng, D.A. Wang, Controllable TiO₂ core-shell phase heterojunction for efficient photoelectrochemical water splitting under solar light, *Appl. Catal. B Environ.* 244 (2019) 519–528.
- [22] M. Shi, G.N. Li, J.M. Li, X. Jin, X.P. Tao, B. Zeng, E.A. Pidko, R.G. Li, C. Li, Intrinsic facet-dependent reactivity of well-defined BiOBr nanosheets on photocatalytic water splitting, *Angew. Chem. Int. Ed.* 132 (2020) 6652–6657.
- [23] M. Li, S.X. Yu, H.W. Huang, X.W. Li, Y.B. Feng, C. Wang, Y.G. Wang, T.Y. Ma, L. Guo, Y.H. Zhang, Unprecedented eighteen-faceted BiOCl with a ternary facet junction boosting cascade charge flow and photo-redox, *Angew. Chem. Int. Ed.* 58 (2019) 9517–9521.
- [24] J. Zhu, F.T. Fan, R.T. Chen, H.Y. An, Z.C. Feng, C. Li, Direct imaging of highly anisotropic photogenerated charge separations on different facets of a single BiVO₄ Photocatalyst, *Angew. Chem. Int. Ed.* 54 (2015) 9111–9114.
- [25] S. Bai, X.Y. Li, Q. Kong, R. Long, C.M. Wang, J. Jiang, Y.J. Xiong, Toward enhanced photocatalytic oxygen evolution: synergistic utilization of plasmonic effect and schottky junction via interfacing facet selection, *Adv. Mater.* 27 (2015) 3444–3452.
- [26] H.F. Li, H.T. Yu, X. Quan, S. Chen, H.M. Zhao, Improved photocatalytic performance of heterojunction by controlling the contact facet: high electron transfer capacity between TiO₂ and the {110} facet of BiVO₄ caused by suitable energy band alignment, *Adv. Funct. Mater.* 25 (2015) 3074–3080.
- [27] P. Li, X.Y. Chen, H.C. He, X. Zhou, Y. Zhou, Z.G. Zou, Polyhedral 30-faceted BiVO₄ microcrystals predominantly enclosed by high-index planes promoting photocatalytic water-splitting activity, *Adv. Mater.* 30 (2018) 1703119.
- [28] S. Bai, L.L. Wang, Z.Q. Li, Y.J. Xiong, Facet-engineered surface and interface design of photocatalytic materials, *Adv. Sci.* 4 (2017) 1600216.
- [29] K.S. Choi, Shape effect and shape control of polycrystalline semiconductor electrodes for use in photoelectrochemical cells, *J. Phys. Chem. Lett.* 1 (2010) 2244–2250.
- [30] C.W. Kim, S.J. Yeob, H.M. Cheng, Y.S. Kang, A selectively exposed crystal facet-engineered TiO₂ thin film photoanode for the higher performance of the photoelectrochemical water splitting reaction, *Energy Environ. Sci.* 8 (2015) 3646–3653.
- [31] A.Y. Zhang, W.Y. Wang, J.J. Chen, C. Liu, Q.X. Li, X. Zhang, W.W. Li, Y. Si, H. Q. Yu, Epitaxial facet junctions on TiO₂ single crystals for efficient photocatalytic water splitting, *Energy Environ. Sci.* 11 (2018) 1444–1448.
- [32] Q.Y. Zeng, J.H. Li, J. Bai, X.J. Li, L.G. Xia, B.X. Zhou, Preparation of vertically aligned WO₃ nanoplate array films based on peroxotungstate reduction reaction and their excellent photoelectrocatalytic performance, *Appl. Catal. B: Environ.* 202 (2017) 388–396.
- [33] S.C. Wang, H.J. Chen, G.P. Gao, T. Butthuree, M.Q. Lyu, S. Thaweesak, J.H. Yun, A. Du, G. Liu, L.Z. Wang, Synergistic crystal facet engineering and structural control of WO₃ films exhibiting unprecedented photoelectrochemical performance, *Nano Energy* 24 (2016) 94–102.
- [34] C.W. Wang, S. Yang, W.Q. Fang, P. Liu, H.J. Zhao, H.G. Yang, Engineered hematite mesoporous single crystals drive drastic enhancement in solar water splitting, *Nano Lett.* 16 (2016) 427–433.
- [35] W.H. Hung, C.J. Peng, C.R. Yang, C.J. Li, J.J. Shyue, P.C. Chang, C.M. Tseng, P. C. Juan, Exploitation of a spontaneous spatial charge separation effect in plasmonic polyhedral α -Fe₂O₃ nanocrystal photoelectrodes for hydrogen production, *Nano Energy* 30 (2016) 523–530.
- [36] M. Meng, X.L. Wu, X.B. Zhu, L. Yang, Z.X. Gan, X.S. Zhu, L.Z. Liu, P.K. Chu, Cubic In₂O₃ microparticles for efficient photoelectrochemical oxygen evolution, *J. Phys. Chem. Lett.* 5 (2014) 4298–4304.
- [37] M. Meng, X.L. Wu, X.B. Zhu, X.S. Zhu, P.K. Chu, Facet cutting and hydrogenation of In₂O₃ nanowires for enhanced photoelectrochemical water splitting, *ACS Appl. Mater. Interfaces* 6 (2014) 4081–4088.
- [38] M. Meng, L. Yang, X.L. Wu, Z.X. Gan, W.Y. Pan, K.L. Liu, C.Y. Li, N. Qin, J. Li, Boosted photoelectrochemical performance of In₂O₃ nanowires via modulating oxygen vacancies on crystal facets, *J. Alloy. Compd.* 845 (2020), 156311.
- [39] L.C. Mu, Y. Zhao, A.L. Li, S.Y. Wang, Z.L. Wang, J.X. Yang, Y. Wang, T.F. Liu, R. T. Chen, J. Zhu, F.T. Fan, R.G. Li, Can Li, Enhancing charge separation on high symmetry SrTiO₃ exposed with anisotropic facets for photocatalytic water splitting, *Energy Environ. Sci.* 9 (2016) 2463–2469.
- [40] S.Q. Su, I. Siretanu, D.V.D. Ende, B. Mei, G. Mul, F. Mugele, Facet-dependent surface charge and hydration of semiconducting nanoparticles at variable pH, *Adv. Mater.* 33 (2021) 2106229.
- [41] X.G. Liu, G.J. Dong, S.P. Li, G.X. Lu, Y.P. Bi, Direct observation of charge separation on anatase TiO₂ crystals with selectively etched {001} facets, *J. Am. Chem. Soc.* 138 (2016) 2917–2920.
- [42] P. Li, Y. Zhou, Z.Y. Zhao, Q.F. Xu, X.Y. Wang, M. Xiao, Z.G. Zou, Hexahedron prism-anchored octahedral CeO₂: crystal facet based homojunction promoting efficient solar fuel synthesis, *J. Am. Chem. Soc.* 137 (2015) 9547–9550.
- [43] C. Li, Y.F. Yu, M.F. Chi, L.Y. Cao, Epitaxial nanosheet-nanowire heterostructures, *Nano Lett.* 13 (2013) 948–953.
- [44] J.A.R. Ramon, A. Cremades, D. Maestre, R.S. Gonzalez, U. Pal, Fabricating necklace-, tower- and rod-shaped In₂O₃ nanostructures by controlling saturation kinetics of catalyst droplets in a vapor-liquid-solid process, *Cryst. Growth Des.* 17 (2017) 4596–4602.
- [45] C.H. Liang, G.W. Meng, Y. Lei, F. Philipp, L.D. Zhang, Catalytic growth of semiconducting In₂O₃ nanofibers, *Adv. Mater.* 13 (2001) 1330–1333.
- [46] S.T. Jean, Y.C. Her, Growth mechanism and photoluminescence properties of In₂O₃ nanotowers, *Cryst. Growth Des.* 10 (2010) 2104–2110.
- [47] Y.G. Yan, Y. Zhang, H.B. Zeng, L.D. Zhang, In₂O₃ nanotowers: controlled synthesis and mechanism analysis, *Cryst. Growth Des.* 7 (2007) 940–943.
- [48] M. Hafeez, T.Y. Zhai, A.S. Bhatti, Y. Bando, D. Golberg, Oxygen vacancy driven modulations in In₂O₃ pyramidal beaded nanowires, *Cryst. Growth Des.* 12 (2012), 4935–4923.
- [49] H.X. Lin, Z.C. Lei, Z.Y. Jiang, C.P. Hou, D.Y. Liu, M.M. Xu, Z.Q. Tian, Z.X. Xie, Supersaturation-dependent surface structure evolution: from ionic, molecular to metallic micro/nanocrystals, *J. Am. Chem. Soc.* 135 (2013) 9311–9314.
- [50] Y.G. Yan, C.Y. Li, L.X. Zhou, W. Xiong, J. Zhang, Regulation of size and uniformity of In₂O₃ nanooctahedra, *Nanoscale* 8 (2016) 13708–13713.
- [51] R.T. Chen, F.T. Fan, C. Li, Unraveling charge-separation mechanisms in photocatalyst particles by spatially resolved surface photovoltage techniques, *Angew. Chem. Int. Ed.* 61 (2022) e202117567.
- [52] R.T. Chen, F.T. Fan, T. Dittrich, Can Li, Imaging photogenerated charge carriers on surfaces and interfaces of photocatalysts with surface photovoltage microscopy, *Chem. Soc. Rev.* 47 (2018) 8238–8262.
- [53] J. Zhu, S. Pang, T. Dittrich, Y.Y. Gao, W. Nie, J.Y. Cui, R.T. Chen, H.Y. An, F.T. Fan, C. Li, Visualizing the nano cocatalyst aligned electric fields on single photocatalyst particles, *Nano Lett.* 17 (2017) 6735–6741.
- [54] R.T. Chen, J. Zhu, H.Y. An, F.T. Fan, Can Li, Unravelling charge separation via surface built-in electric fields within single particulate photocatalysts, *Faraday Discuss.* 198 (2017) 473–479.
- [55] T. Takata, J.Z. Jiang, Y. Sakata, M. Nakabayashi, N. Shibata, V. Nandal, K. Seki, T. Hisatomi, K. Domon, Photocatalytic water splitting with a quantum efficiency of almost unity, *Nature* 581 (2020) 411–414.
- [56] S. Lardhi, L. Cavallo, M. Harb, Significant Impact of exposed facets on the BiVO₄ material performance for photocatalytic water splitting reactions, *J. Phys. Chem. Lett.* 11 (2020) 5497–5503.
- [57] L.L. Wang, J. Ge, A.L. Wang, M.S. Deng, X.J. Wang, S. Bai, R. Li, J. Jiang, Q. Zhang, Y. Luo, Y.J. Xiong, Designing p-Type Semiconductor-metal hybrid structures for improved photocatalysis, *Angew. Chem. Int. Ed.* 53 (2014) 5107–5111.
- [58] M. Wu, W.J. Chen, Y.H. Shen, F.Z. Huang, C.H. Li, S.K. Li, In situ growth of matchlike ZnO/Au plasmonic heterostructure for enhanced photoelectrochemical water splitting, *ACS Appl. Mater. Interfaces* 6 (2014) 15052–15060.
- [59] F.C. Lei, Y.F. Sun, K.T. Liu, S. Gao, L. Liang, B.C. Pan, Y. Xie, Oxygen vacancies confined in ultrathin indium oxide porous sheets for promoted visible-light water splitting, *J. Am. Chem. Soc.* 136 (2014) 6826–6829.
- [60] J.Y. Gan, X.H. Lu, J.H. Wu, S.L. Xie, T. Zhai, M.H. Yu, Z.S. Zhang, Y.C. Mao, S. C. Wang, Y. Shen, Y.X. Tong, Oxygen vacancies promoting photoelectrochemical performance of In₂O₃ nano-cubes, *Sci. Rep.* 3 (2013) 1021.
- [61] M.Y. Li, H. Liu, Y.H. Song, J.J. Gao, Design and constructing of mutually independent crystal face exposed TiO₂ homojunction and improving synergistic effects for photoelectrochemical hydrogen generation and pollutant degradation, *Int. J. Energy Res.* 42 (2018) 4625–4641.
- [62] M. Ye, J. Gong, Y. Lai, C. Lin, Z. Lin, High-efficiency photoelectrocatalytic hydrogen generation enabled by palladium quantum dots-sensitized TiO₂ nanotube arrays, *J. Am. Chem. Soc.* 134 (2012) 15720–15723.